Seismoacoustic recovery of the SpaceX CRS-32 Dragon re-entry with a proof-of-concept for automated detection

Mikel Taotao Yu[a,b,*], Benjamin Fernando[b]

[a] Department of Applied Mathematics and Computer Science, Technical University of Denmark, Richard Petersens Plads, Building 324, DK-2800 Kgs. Lyngby, Denmark

[b] Department of Earth and Planetary Sciences, Johns Hopkins University, 3400 North Charles Street, Baltimore, 21211, Maryland, USA

[*] Corresponding author

This manuscript is a non-peer reviewed preprint submitted to EarthArXiv. It has also been submitted for peer review to *Acta Astronautica* (Elsevier). This preprint has not yet been peer reviewed.

Corresponding author ORCID: https://orcid.org/0009-0007-1071-7258

Corresponding author email: s234812@dtu.dk

Graphical Abstract

Seismoacoustic recovery of the SpaceX CRS-32 Dragon re-entry with a proof-of-concept for automated detection

Mikel Taotao Yu, Benjamin Fernando

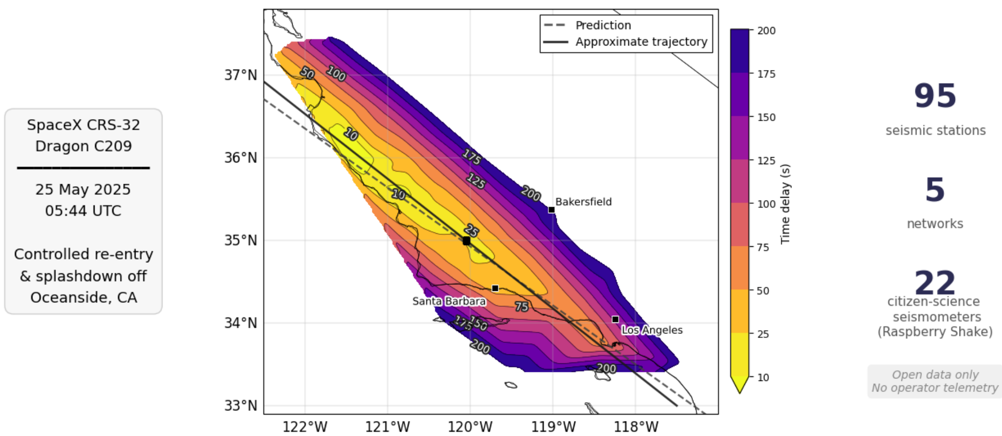

Highlights

Seismoacoustic recovery of the SpaceX CRS-32 Dragon re-entry with a proof-of-concept for automated detection

Mikel Taotao Yu, Benjamin Fernando

- Independent trajectory recovery of a controlled SpaceX Dragon re-entry
- 95 open-access seismic stations across five networks used for localization
- Citizen-science Raspberry Shake instruments contribute 23% of the dataset
- Results consistent with operator-published splashdown corridor
- No operator telemetry or classified data required
- Neural network trained on two events demonstrates potential for automated picking

Seismoacoustic recovery of the SpaceX CRS-32 Dragon re-entry with a proof-of-concept for automated detection

Mikel Taotao Yu[a,b,*], Benjamin Fernando[b]

[a] *Department of Applied Mathematics and Computer Science, Technical University of Denmark, Richard Petersens Plads, Building 324, Lyngby, 2800, Lyngby-Taarbæk, DK*
[b] *Department of Earth and Planetary Sciences, Johns Hopkins University, 3400 North Charles Street, Baltimore, 21211, Maryland, USA*

Abstract

Atmospheric re-entries of human-made objects are increasing in frequency, yet detailed information on their trajectory, fragmentation, and debris footprint is rarely made publicly available. This creates an information asymmetry in which regulators, independent agencies, and the scientific community lack the means to verify that re-entries occurred as reported or to characterize their physical processes for future modeling. We address this gap by applying a seismoacoustic localization method to the 25 May 2025 re-entry of the SpaceX CRS-32 Cargo Dragon spacecraft which splashed down in the Pacific Ocean off the coast of Southern California. Using openly available seismic waveform data from 5 networks, including 22 Raspberry Shake amateur instruments, we recover a re-entry trajectory consistent in trajectory with the operator's publicly communicated splashdown prediction and release the manually labeled CRS-32 labeled N-wave picks as a public dataset. As a preliminary step toward automation, we train a neural network on the manually picked dataset and demonstrate reliable onset detection with stable performance across a wide range of detection thresholds, showcasing promise for N-wave detection from a two-event training set. These results show that existing open seismic infrastructure can provide independent, continental-scale characterization of re-entry events: a capability increasingly needed as the rate and opacity of commercial re-entries continue to grow.

*Corresponding author
Email address: `s234812@dtu.dk` (Mikel Taotao Yu)

Keywords: Atmospheric re-entry, Seismic detection, Sonic boom, Space situational awareness, Citizen science seismology, Machine learning

1. Introduction

Human spaceflight in low Earth orbit is becoming increasingly routine [1]. The International Space Station, China's Tiangong station, and planned commercial stations all require regular crew rotation, cargo resupply, and hardware disposal — each of which involves an atmospheric re-entry. Some of these re-entries are controlled, such as crew capsules and cargo spacecraft executing deliberate deorbit burns toward predetermined splashdown zones. Others are uncontrolled, such as jettisoned service modules and decommissioned hardware that decay naturally from orbit without active guidance over where or when they re-enter. As human spaceflight operations expand through NASA and China's Commercial Crew Program and new commercial stations, the frequency of both types of re-entry will continue to grow.

Therefore, the ability to independently track and characterize these re-entry events is essential: not only for assessing debris risk, but also for determining broader impacts such as the number of people exposed to sonic booms, airspace disruption, and the environmental effects of re-entry emissions. Yet the characterization of re-entry events depends almost entirely on telemetry retained by the operator; details of actual trajectory, fragmentation dynamics, and debris footprint are rarely released publicly. This introduces an information asymmetry where regulators, independent agencies, and the scientific community are unable to verify re-entries occurring as reported or characterizing their physical processes for future modeling. The regulatory framework itself reveals this gap: the FAA does not mandate controlled disposal of rocket upper stages at the end of launch operations, and has acknowledged that its assessment of re-entry risk from large constellations depends substantially on operator-reported demisability claims that have not been independently verified [2]. Recent findings have further questioned the accuracy of such analyses for several spacecraft types [3], further emphasizing the importance of independent verification.

Existing ground-based tracking methods cannot close this verification gap. Optical observations are line-of-sight limited and radar data with over-the-horizon visibility are generally classified [4, 5]. Even the best operational predictions exceed ±10% timing error in over 40% of cases [6]. For objects burning up during re-entry, this limits the ability to validate demisability predictions and calibrate break-up models against real events. For objects such as crew capsules and cargo spacecraft, that survive to the ground, it limits understanding of sonic boom impact on affected populations, environmental exposure along the re-entry corridor, and the accuracy of predicted splashdown locations used to coordinate recovery operations and maritime safety zones.

Seismometers and infrasound sensors offer an independent, observation-based alternative. Re-entering objects generate low-frequency acoustic waves that couple into the ground and can be recorded by seismometers within a few hundred kilometres of the source [7], while dedicated infrasound sensors can detect signals at substantially greater distances [4]. Crucially, this infrastructure, that was originally deployed for earthquake monitoring and nuclear test verification, is openly accessible and provides continental-scale coverage at no additional cost.

In this work, we apply the seismoacoustic localization method introduced by Fernando and Charalambous [8] to the controlled re-entry of the SpaceX CRS-32 Cargo Dragon spacecraft on 25 May 2025. Unlike the uncontrolled rocket-body re-entry studied by Fernando and Charalambous, this event was a controlled splashdown off the California coast, with the trajectory passing mostly over the Pacific Ocean where few seismic stations exist. Additionally, as a preliminary step toward operational scalability, we explore the feasibility of automated N-wave detection by fine-tuning two pre-trained seismic foundation models on the manually picked dataset produced by this study.

1.1. The May 2025 SpaceX CRS-32 Capsule re-entry

On May 25, 2025, at 05:44 UTC, the SpaceX Cargo Dragon spacecraft (capsule C209, NORAD ID 63628) concluded NASA's 32nd Commercial Resupply Services mission with a controlled re-entry and splashdown in the Pacific Ocean off the coast of Oceanside, California [9, 10]. The Dragon 2 capsule has a diameter of 4.0 m [11] and a return payload mass of approximately 1,870 kg from the International Space Station [9]; note that this cargo mass is distinct from the capsule's own re-entry mass (structure plus residual propellant), which is not publicly disclosed by the operator to sufficient precision for this analysis.

For several reasons, this event serves as a valuable case study. First, while seismoacoustic methods have previously been applied to Space Shuttle re-entries [12, 13], meteorite fireballs [14], uncontrolled rocket-body re-entries [8, 15], and intact sample return capsules [16, 17, 18, 19, 20, 21], no published study has applied them to a commercial crew-class capsule: a vehicle type that will become increasingly common as human spaceflight operations expand. Return capsules are structurally rigid, non-ablating bodies that, like a crew capsule, do not disintegrate during descent as is characteristic of space debris. However, they differ in a key distinction that is relevant for this case study: They follow ballistic, non-propulsive trajectories at hyperbolic return velocities of 11–12 km/s, essentially indistinguishable from meteoroid entries in this regard. A crew-class capsule such as Dragon instead executes a propulsively controlled deorbit burn and guided descent from low earth orbit at approximately 7.8 km/s, followed by parachute-assisted splashdown. This combination of a controlled, guided trajectory and an intact, fixed-shape re-entry vessel has not previously been addressed by seismoacoustic methods. Second, unlike the uncontrolled re-entry studied by Fernando and Charalambous, the CRS-32 mission was a controlled splashdown for which no public trajectory data is available, placing it in precisely the regime where independent verification is most needed. Third, the coastal splashdown means that part of the trajectory lies over the Pacific Ocean where no seismic stations exist, testing the method under a geometrically constrained configuration that is representative of future capsule recovery operations.

1.2. Shockwave Generation

During atmospheric re-entry, a given spacecraft is traveling at hypersonic speeds, conventionally defined as Mach $\gtrsim 5$. As it descends, the increasing atmospheric density allows its shockwave to propagate down to the ground as a sonic boom. The seismic expression of this boom is an N-wave: a sharp pressure increase from the leading shock, a linear decline, and a sharp pressure decrease from the trailing shock, producing a characteristic 'N' shaped impulsive signature on vertical-component seismograms picked up by stations near the trajectory line [22]. On seismometers this manifests as an down-up polarity as the leading compressional shock first pushes the ground downward. On the corresponding infrasound signal, a direct pressure measurement, it displays the opposite up-down signature since the leading shock is recorded as a positive overpressure [17].

Because the shockwave is generated continuously along the hypersonic trajectory, each station records the arrival of the N-wave at a time determined primarily by its distance from the nearest point on the trajectory and the path speed of sound. A secondary contribution arises from the motion of the source itself: stations downrange of the spacecraft receive the signal slightly earlier than those uprange, since the object is advancing toward them. However, because the spacecraft velocity far exceeds the speed of sound, this along-track effect is small relative to the perpendicular acoustic propagation time. Together, the pattern of differential arrival times across a network of stations constrains the ground-track geometry. By recording a sufficient number of arrival times across a network of stations, it is therefore possible to recover the trajectory of the spacecraft, including its horizontal extent (size), the ratio of along-track to cross-track dimensions (aspect ratio) and the descent angle of the re-entering body [8].

2. Methods

2.1. Data Acquisition

To identify N-waves originating from the re-entry, waveform data were downloaded and processed using `ObsPy`, a Python library for seismology [23, 24]. Using its mass downloader method, station metadata was retrieved from the FDSN web services Earthscope Consortium (formerly known as IRIS, now merged with UNAVCO), Southern California Earthquake Data Center (SCEDC), and Northern California Earthquake Data Center (NCEDC) [25, 26, 27]. The search domain was centered near Santa Barbara (34.42°N, 119.70°W), approximately midway along the expected re-entry corridor, with a radius of 3.6° ($\sim$400 km), roughly twice the distance at which previous work suggests that direct sonic booms are detectable seismically [7].

Vertical-component ground velocity data were requested over a one-hour window from 05:00 to 06:00 UTC on 25 May 2025, encompassing the expected re-entry and allowing sufficient margin for potentially later-arriving signals at distant stations. Vertical-component data were used exclusively, as acoustic-to-seismic coupling from a near-vertically incident shockwave predominantly excites vertical ground motion [17]; horizontal components are dominated by secondary, ground-coupled propagation effects and offer little additional information to the direct N-wave arrival. This choice is also consistent with the instrument availability across the network, as a sizable fraction of stations, including all Raspberry Shake citizen-science instruments, only record the vertical channel.

Data were obtained from five seismic networks: Southern California Seismic network (CI) [28], Berkeley Digital Seismograph Network (BK) [29], ANZA Regional Network (AZ) [30], USGS Northern California Seismic Network (NC) [31], and Raspberry Shake citizen-science network (AM) [32]. Stations are identified throughout this paper using the standard FDSN naming convention `NET.STA`, where `NET` is the two-letter network code and `STA` denotes the station identifier (e.g., BK.LAND is the station LAND of the Berkeley Digital Seismic Network).

2.2. Signal Processing and N-wave identification

The seismic data had their instrument response removed and were then bandpass-filtered in the interval of 1 to 18 Hz to suppress microseismic noise below 1 Hz and to retain the sub-audible frequency bands in which the N-wave energy is concentrated. Afterwards, each signal was manually inspected for plausible N-waves. For each identified event, the arrival time of the earliest clear onset (not the peak amplitude) was selected. Where a station provided picks on multiple channels, a fixed channel preference in the following order was applied: BHZ (broadband, 20–40 samples/s), HHZ (high-broadband, 100 samples/s), and EHZ (short-period, 100 samples/s). BHZ channels offer the broadest frequency response, making them the preferred choice if available. HHZ provides comparable bandwidth at higher sampling rates while EHZ channels, typical of Raspberry Shake instruments, have a narrower frequency response but still retain adequate sensitivity in the 1-18 Hz band used in this study. However, these amateur-operated stations are often deployed in non-optimal settings (e.g. inside homes) and consequently exhibit higher background noise (see Appendix C). Generally, they also lack the professional calibration of institutional networks. Hence, onset times from EHZ channels were interpreted with more caution.

After manual waveform inspections and deduplication of stations appearing across multiple channels, 95 unique stations contributed to the final analysis. Of those, 42 stations were obtained from CI, 26 from BK, 22 from AM, 3 from NC, and 2 from AZ. Representative examples of seismograms from five stations are displayed here:

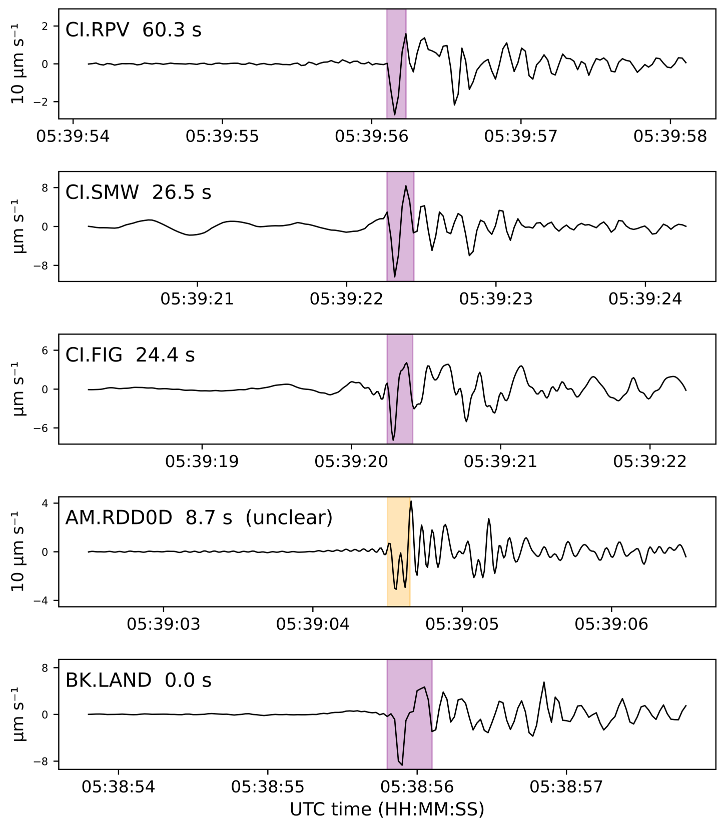

Figure 1: Seismograms from five stations illustrating typical N-wave arrivals from the re-entry sonic boom. Four stations (all except AM.RDD0D) show clear N-wave signals, highlighted in purple; minor waveform differences between them likely reflect variations in local geology, atmospheric conditions, and propagation distance. A lower-amplitude reverberatory coda is visible following the initial N-wave at several stations consistent with secondary ground-coupled arrivals reported in previous re-entry observations [17]. Station AM.RDD0D (highlighted in yellow) displays a distinct arrival at the expected time but lacks a well-developed N-wave shape, likely due to the higher noise and less shielded installation typical of amateur-operated instruments. It is included because its arrival time matches the pattern seen at clearer stations, while its ambiguous waveform illustrates the difficulty of manual phase identification. Note the different temporal and velocity scales between panels.

Fig. 1 shows 5 seismograms with their N-waves manually annotated. Of them, 4 are highlighted in purple to convey that the N-wave is clear and unambiguous. The station AM.RDD0D is instead highlighted in yellow as its N-wave is unclear. Signals like these show that the exact arrival time and duration of an N-wave can be ambiguous and difficult to distinguish from other noise signals picked up by the seismometer. Hence, the picking process is prone to judgment and measurement errors and standardized, automated picking architectures offer advantages of consistency at the very least.

An N-wave coupling into the ground produces a signal that is short in duration and hence broad in frequency content, resulting in a sudden, broadband increase in spectral power on a spectrogram. Because this broadband spike occurs simultaneously with the spike on the seismogram, cross-referencing the two representations increases pick confidence. We therefore inspected corresponding spectrograms as well for all arrivals, illustrated on the ten closest stations in Fig. 2. This displays a record section of the ten stations closest to the trajectory to show the coherent move-out of the sonic boom arrival across the network, and to demonstrate how spectrograms are used to confirm the timing of these short, broadband signals.

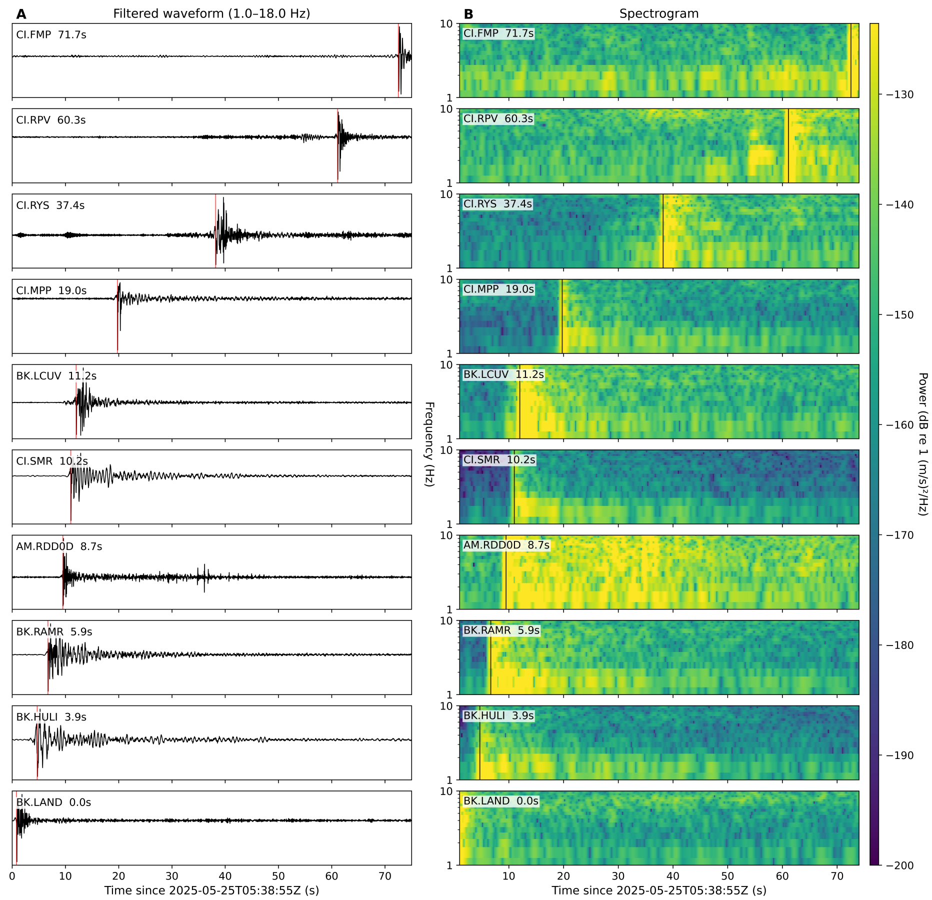

Figure 2: **Examples of seismic data recorded from the re-entry event. (A)** seismograms of the ten closest stations to the recovered trajectory. The possible arrival times of the N-wave are marked with a vertical red line. **(B)** Spectrograms of the same 10 stations in the interval of 1-18 Hz. The vertical axis denotes frequency in Hz. Power spectral densities are expressed in decibels relative to 1 $(\mathrm{m/s})^2/\mathrm{Hz}$. Once again the possible arrival times are marked with a vertical line.

2.3. Elevation Correction

Stations located at elevation z would receive the signal earlier than a hypothetical sea-level station at the same geographical position. The observed travel time τ_{obs} is therefore shorter than the travel to the sea-level reference by approximately z/c where c denotes the assumed speed of sound. To remove this elevation effect and project all stations onto a common horizontal plane, we applied the following correction:

$$\tau_{\text{corr}} = \tau_{\text{obs}} + \frac{z}{c} \tag{1}$$

Here, a value of $c = 330$ m/s was chosen for computations. Adding the term z/c in Eq. 1, compensates for the extra vertical distance the signal would traverse to reach sea level. As such, τ_{corr} is the travel time that would be observed at sea level. After this correction, differences in τ_{corr} would reflect only horizontal propagation distance without elevation bias. Because the elevation corrections are small, any variation of the sound speed with altitude is negligible in this context, making a constant c sufficient. Corrections ranged from 0.10 s for near sea-level coastal stations to 5.98 s for the highest-elevation station (CI.ABL, 1975 m), confirming the inclusion of the correction as non-negligible for stations located on inland mountains in the Southern California Network.

2.4. Trajectory estimation

To estimate the propagation direction of the airwave, a structure-tensor analysis [33] was applied to the interpolated delay field. Structure tensors have been widely used in seismic data processing to estimate wavefront and reflector orientations from spatial gradient fields [34]. The method was chosen for its robust estimate of the dominant wavefront propagation direction even under irregular station spacing and without requiring explicit velocity modeling. First, all N-wave arrivals were defined as delay times relative to the earliest arrival at 05:38:55 UTC at Big Sur (Station BK.LAND) in the California Central Coast. At each grid point, the spatial gradient of the delay surface was denoted as $(\partial T/\partial x, \partial T/\partial y)$. Based on that, the following 2×2 structure tensor was formed,

$$J = \begin{bmatrix} \langle g_x, g_x \rangle & \langle g_x, g_y \rangle \\ \langle g_x, g_y \rangle & \langle g_y, g_y \rangle \end{bmatrix} \tag{2}$$

Where g_x and g_y denote the horizontal and vertical components of the delay gradients, respectively. $\langle \cdot, \cdot \rangle$ denotes the weighted spatial average within the contours of the station network. In order to emphasize regions containing plenty of well-defined delay gradients, each grid point was weighted by its gradient magnitude. The eigenvector corresponding to the largest eigenvalue of J yielded the dominant gradient direction; in other words, the direction along which arrival delays increased most rapidly, approximately perpendicular to the spacecraft ground track. The inferred trajectory was therefore taken as the perpendicular to this gradient direction, oriented westward from the California coast, displayed on Fig. 3.

Finally, N-wave durations were measured and plotted against downrange distance from the earliest-arriving station (BK.LAND). Results are presented in Section 3 and briefly interpreted in the context of Whitham's quarter-power scaling law in Section 4.3 (see Appendix A for full discussion).

2.5. Automated N-wave picking with pre-trained machine learning models

Recent work has investigated deep-learning approaches for to identify seismic waves generated by meteor entries and obtained promising results [35]. To explore the potential of automated N-wave detection for controlled capsule re-entries, two pre-trained seismic phase pickers, SeisLM and PhaseNet [36, 37], were fine-tuned on a combined dataset of manually labeled waveforms from two spacecraft reentry events: the SpaceX Dragon CRS-32 reentry (25 May 2025, 95 stations) and the Shenzhou-15 reentry (2 April 2024, 125 stations) from the event studied by Fernando and Charalambous [8]. Both models were originally trained on large catalogues of earthquake phase arrivals; here, their final layers were re-trained to predict N-wave onset (t_A) and end (t_B) times instead. Each architecture was evaluated in two initialization configurations, giving four model variants in total.

Each station's waveform was extracted as a 30 second window centered on the expected arrival and resampled to 100 Hz. Ground-truth pick times were encoded as Gaussian probability targets ($\sigma = 0.10\,\text{s}$) centered at the manually picked t_A and t_B samples. The models output a probability curve for each phase, from which the sample with the highest probability was taken as the predicted pick time. Of the total 220 labeled stations, 22 were held out as a fixed test set (12 from Shenzhou-15, 10 from Dragon CRS-32), stratified by event so that both reentries were represented proportionally. The remaining 198 stations were used for five-fold cross-validation, stratified by event, yielding approximately 158 training and 40 validation stations per fold. To counteract the small dataset size, data augmentation was applied during training: random time shifts ($\pm 5\,\text{s}$), amplitude jitter ($\pm 15\,\%$), and additive Gaussian noise. Unclear picks were upsampled by a factor of two via weighted random sampling to prevent the training signal being dominated by high-confidence examples. Training was performed on an NVIDIA A100-PCIE-40 GB GPU.

PhaseNet is a U-Net convolutional architecture originally trained on earthquake P- and S-wave arrivals. Two initializations were tested: (i) *PhaseNet (pretrained)*, loaded from the published earthquake catalogue weights, and (ii) *PhaseNet (scratch)*, initialized with random weights and then trained entirely on the N-wave dataset. Both variants used a batch size of 16, which denotes the amount of waveform segments processed together before each parameter update. For each parameter update, the learning rate was set to 10^{-4} which controls the step size, determining how much the network's internal parameters are adjusted after each batch of training samples. For every time sample, the network outputs a probability that it corresponds to a signal onset, a signal end, or a background noise. Because true onset and end samples are vastly outnumbered by noise samples in any given waveform, we applied a pick-loss weight of 10.0, which up-weights the onset and end channels relative to the noise channel to counteract this class imbalance and prevent the model from trivially prediciting 'noise' everywhere.

SeisLM is a transformer-based foundation model pretrained on diverse seismic waveforms. Again, two fine-tuning strategies were tested: (i) *SeisLM (frozen CNN)*, in which the convolutional feature extractor was frozen and only the transformer layers and classification head were updated, and (ii) *SeisLM (full)*, in which all weights were updated. Both variants used a learning rate of 5×10^{-5} and batch size of 8.

All models were trained for up to 1000 epochs with early stopping (patience = 100 epochs) and a ReduceLROnPlateau schedule that halved the learning rate after ten consecutive epochs without validation loss improvement, down to a minimum of 10^{-7}. Model performance was evaluated using mean absolute error (MAE) and signed bias for both t_A and t_B, within-tolerance detection fractions at 0.05 s, 0.10 s, and 0.50 s, and F_1 score: the harmonic mean of precision and recall, where a true positive was defined as a detected pick within 0.05 s of the manual reference. Results are displayed in Tables 1, 2, and 3.

2.5.1. Model Evaluation Metrics

To assess the N-wave detection capabilities of the trained models, the standard classification metrics precision and recall were employed. Precision is defined as,

$$\text{Precision} = \frac{\text{True Positives}}{\text{True Positives} + \text{False Positives}} \tag{3}$$

Precision measures the accuracy of positive predictions by giving the ratio of true positives to the total amount of positive predictions. In other words, it specifies the correctness of instances labeled as positive. Recall is defined as follows,

$$\text{Recall} = \frac{\text{True Positives}}{\text{True Positives} + \text{False Negatives}} \tag{4}$$

As Equation 4 implies, recall measures the proportion of actual positive instances that are correctly identified by the model. Given the goal objective of re-entry localization, two workflow implementations can be considered:

- For a fully automated pipeline with machine picked N-waves, a high precision is crucial as incorrect signals will degrade the interpolation map. Conversely, recall is not as important since complete detection of all N-waves is not required. The metric only needs to be high enough to provide enough picks for sufficient coverage for the contour map.

- For a human-in-the-loop pipeline, manual verification of machine annotations absorbs the cost of false positives. Therefore, a lower precision becomes acceptable in favor of higher recall, maximizing the number of candidate picks presented for review.

Regardless of pipeline, however, these precision and recall thresholds are not uniform across stations. A missed or incorrect pick at an azimuthally unique station costs more than a mistake at a station with nearby neighbours. Furthermore, given that the interpolation map is constructed from delays relative to the first arrival, the correctness of this specific station is more consequential than all other picks. Any machine learning-based workflow should keep these points in mind during implementation.

2.6. Software

Data processing was done with ObsPy [23, 24]. Numerical analysis was carried out with NumPy [38]. Figures were produced with Matplotlib [39] and Cartopy [40].

3. Results

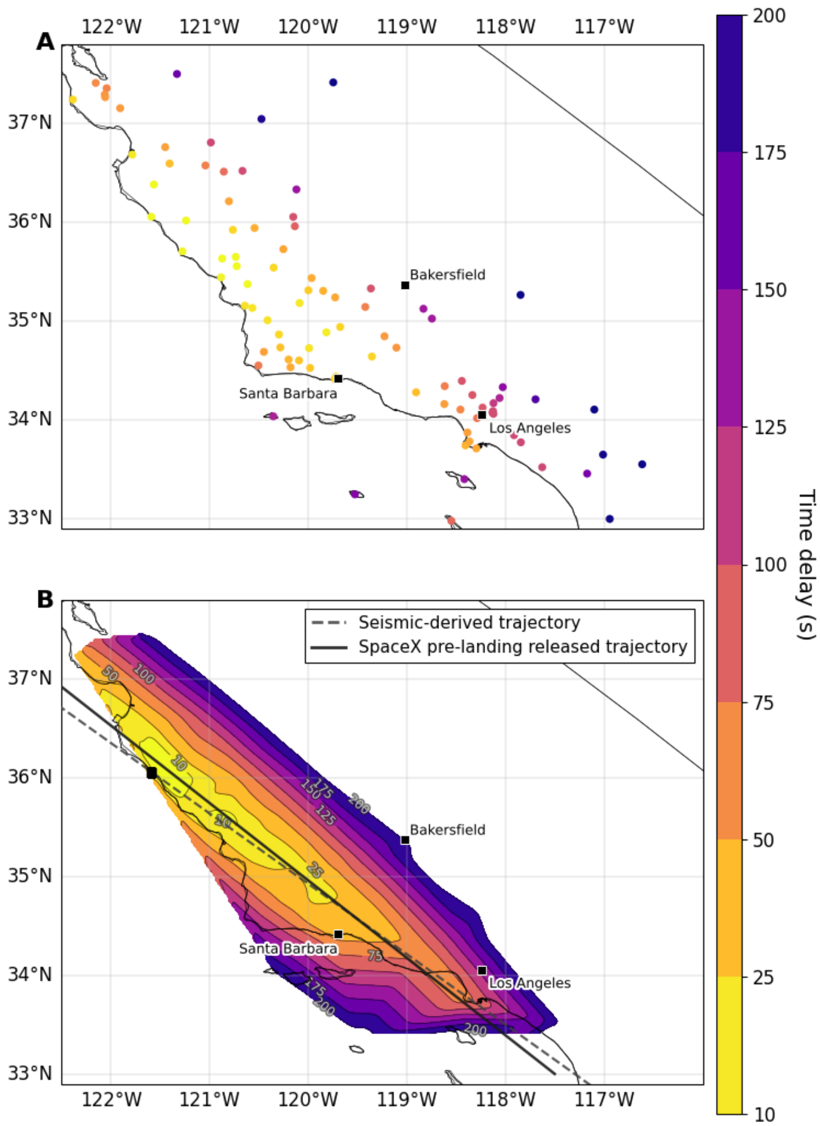

Figure 3: **Pointwise and interpolated arrival times of sonic booms at stations across these networks.** **(A)** A map of stations recording the sonic boom related to the event, color-coded by time delay relative to the first arrival, BK.LAND (increasing from yellow to purple). **(B)** A linearly interpolated contour map of arrival times, with a gradient-based fit (dashed gray line) and an approximate trajectory based on the SpaceX release of the trajectory that remains to be validated or confirmed (solid black line).

3.1. Performance of Machine Learning Models

Below are the results for the PhaseNet and SeisLM configurations. The strongest results are marked in **bold**. The columns showing $\leq x.xx\ s$ denotes the fraction of annotated stations that received a pick within $x.xx$ seconds of the manual annotation.

Table 1: 5-fold cross-validation results (mean ± std over folds). F_1 at 0.05 s tolerance.

	Onset (tA)					End
Model	Val loss	MAE (s)	≤0.10 s	≤0.50 s	F_1	F_1
PhaseNet (pretrained)	4.788 ± 0.012	13.13 ± 0.17	0.000	0.000	—	—
PhaseNet (scratch)	0.129 ± 0.021	**0.345 ± 0.113**	**0.459 ± 0.071**	**0.839 ± 0.062**	**0.323 ± 0.093**	0.165 ± 0.084
SeisLM (frozen CNN)	0.134 ± 0.007	1.124 ± 0.598	0.339 ± 0.061	0.536 ± 0.083	0.275 ± 0.065	0.298 ± 0.078
SeisLM (full fine-tune)	0.134 ± 0.010	1.228 ± 0.579	0.318 ± 0.057	0.581 ± 0.052	0.296 ± 0.079	0.241 ± 0.079

Table 2: Held-out test set results (22 stations). Detection threshold 0.20; F_1 at 0.05 s tolerance.

	Onset (tA)							End
Model	MAE (s)	Bias (s)	P	R	F_1	≤0.10 s	≤0.50 s	F_1
PhaseNet (pretrained)	13.30	−13.30	0.000	—	—	0.000	0.000	—
PhaseNet (scratch)	**0.197**	**+0.080**	**0.545**	**1.000**	**0.706**	**0.682**	**0.864**	0.174
SeisLM (frozen CNN)	0.542	+0.286	0.211	0.571	0.308	0.364	0.591	0.250
SeisLM (full fine-tune)	0.475	+0.207	0.421	0.727	0.533	0.455	0.591	**0.250**

Table 3: Detection-threshold sweep for PhaseNet (scratch) on the held-out test set (22 stations). F_1 computed at 0.05 s tolerance. Recall computed using a fixed 0.05 seconds criterion. $F_1 = 0.706$ is stable across the full range 0.05–0.70; only at 0.80 do correctly-placed picks begin to be missed.

	Onset (tA)							End (tB)		
Thr.	P	R	F_1	≤0.05 s	≤0.10 s	≤0.50 s	Det.	P	R	F_1
0.05	0.545	1.000	**0.706**	0.545	0.682	0.864	1.00	0.095	1.000	0.174
0.20	0.545	1.000	**0.706**	0.545	0.682	0.864	1.00	0.095	1.000	0.174
0.40	0.545	1.000	**0.706**	0.545	0.682	0.864	1.00	0.095	1.000	0.174
0.60	0.632	0.800	**0.706**	0.545	0.682	0.818	0.86	0.105	0.500	0.174
0.70	0.667	0.750	**0.706**	0.545	0.682	0.773	0.82	0.118	0.333	0.174
0.80	0.727	0.421	0.533	0.364	0.455	0.455	0.50	0.167	0.182	0.174

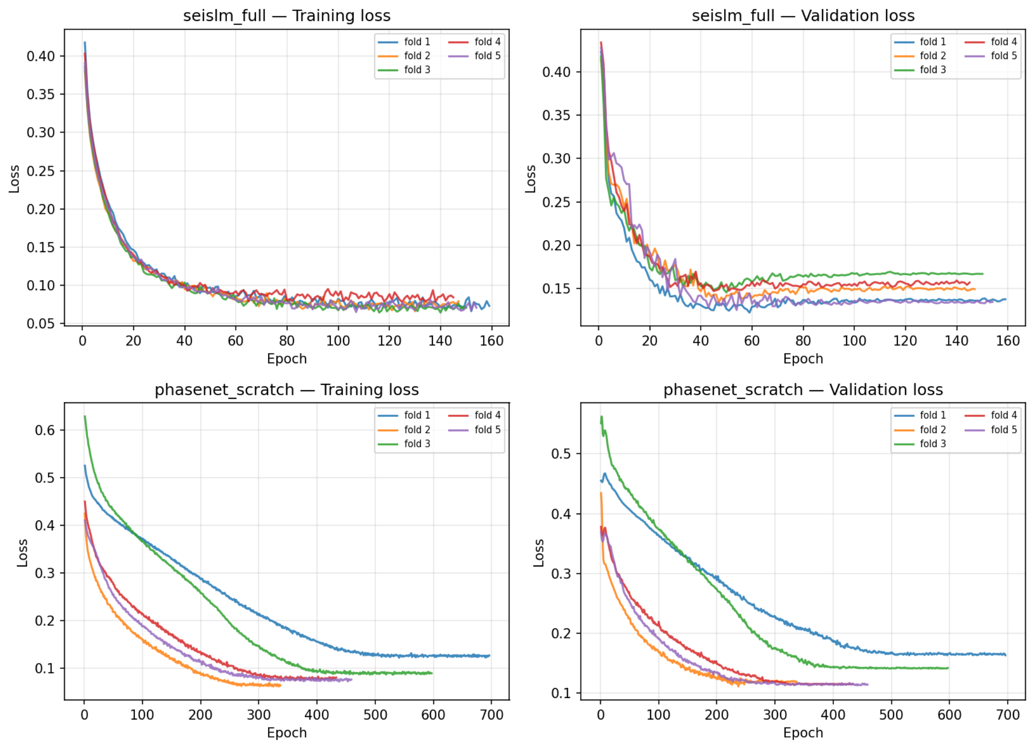

Figure 4: Learning curves of PhaseNet (scratch) and seisLM (full fine-tune), the two best performing models. For each validation fold, the training loss is computed against the iterations of training epochs

4. Discussion

4.1. Trajectory recovery and validation

A trajectory recovery of the re-entry is displayed in Fig. 3. The structure-tensor analysis of its interpolated delay field yields the dominant direction along which N-wave arrival times increase most rapidly across the station network. Because the signal propagating outward at the local speed of sound, and each station receives the sonic boom from the acoustically nearest point on the trajectory, the arrival delays are governed primarily by each station's perpendicular distance to the ground track. The dominant gradient direction therefore points approximately perpendicular to the re-entry trajectory. The inferred ground track, taken as the perpendicular to this gradient, crosses the California coast from northwest to southeast and extends westward over the Pacific Ocean, consistent with the publicly communicated splashdown corridor off the coast of Oceanside, California [10].

Qualitatively, the reconstructed trajectory's azimuth and approximate splashdown site in the Pacific Ocean are consistent with the pre-splashdown recovery graphic released by SpaceX [41]. However, detailed telemetry such altitude, velocity, and precise timing for this re-entry has not been made publicly available. As a result, a quantitative validation against an independent ground-truth trajectory is not currently possible for this controlled re-entry. Agreement therefore relies on the spatial consistency of the independently observed N-wave arrivals and delay field geometry which displays a well-defined, smoothly varying pattern with low scatter. This indicates that the recovered track is a robust representation of the actual shockwave footprint. Future re-entries with available telemetry could provide the quantitative validation needed assess method accuracy and calibration.

4.2. Limitations

Several limitations should be noted. First, all N-wave picks were first identified through manual inspection. This is a time consuming process that carries a risk of measurement error. The uncertainty is further compounded by seismogram morphology being sensitive to bandpass filtering-choices and substantial background noise in populated areas. Automated or semi-automated picking methods could improve efficiency and reproducibility, which is further discussed in Section 4.4 and Appendix B.

Second, the CRS-32 re-entry event splashed down near the California coast, leaving the oceanward side of the trajectory without seismic stations. This asymmetry reduces spatial coverage of the countour map on that side, meaning that the interpolated surface is well constrained only within the convex hull of the station network, close to the coastline. The seismic-derived trajectory itself, however, is obtained by fitting a line through the arrival-time data and is therefore extrapolated beyond this station-constrained region, out over the Pacific Ocean. Despite this extrapolation, the recovered ground track remains consistent with SpaceX's independently released trajectory well offshore, demonstrating that the method's trajectory estimate does not depend on having station coverage at every point along the path. The inclusion of Raspberry-Shake (AM) stations proved important for increasing the density of inland coverage. The consistency of the delay-time field suggests that the technique is robust despite this constraint; an encouraging outcome for future re-entries occuring over the ocean, provided a sufficient coastal or island network exists nearby.

4.3. Whitham's theory and N-wave duration

As an independent consistency check, we compared measured N-wave durations against several distance proxies to test whether they follow Whitham's scaling relation [22, 12]. No reliable correlation was obtained (all $R^2 \leq 0.31$), largely because none of the proxies accurately represents the true slant range from the shock front, and because our stations are in the acoustic far field where propagation effects distort the source waveform. The analysis also highlights the need for trajectory altitude and Mach number data for a meaningful test. A full discussion containing a description of the proxies, the underlying theory, and the far-field argument is provided in Appendix A.

4.4. Applied Machine Learning for N-wave detection

The manual picking carried out in this study, while effective, was time-consuming and subject to operator judgment. This was particularly evident for stations with low SNR or ambiguous waveform morphology, hence the motivation behind exploring machine picked N-waves. From the test-set results, the pretrained PhaseNet performed the worst, likely explained by the difference of its source domain and the target task at hand. PhaseNet's convolutional weights encode features tuned to impulsive, broadband P- and S-wave arrivals recorded over short windows, where the onset is typically sharp and arrives near the start of the window. N-waves produced by spacecraft reentries are acoustic rather than seismic in origin: they are lower-frequency, arrive gradually, and are embedded in a fundamentally different noise background. The pretrained feature extractor therefore responded to whatever transient in the window most resembled a seismic onset, producing a systematic -13 s bias irrespective of the true N-wave location. Removing the pretrained weights completely resolved this: PhaseNet trained from random initialization on 220 N-wave examples achieved a test F_1 of 0.706 at 50 ms tolerance and a MAE of 0.197 s, confirming that the U-Net architecture transfers well to N-wave picking even though its pretrained knowledge does not.

A practically significant test result is that PhaseNet (scratch) achieved a recall of 1.00 for every detection threshold between 0.05 and 0.70 (Table 3). In a deployment scenario, a threshold in this range would flag every station that recorded an N-wave without missing any, at the cost of a precision of 0.55. The implication of this would be that roughly one in two flagged waveforms would require a human analyst to confirm or reject. Compared to manually screening the full seismic network, this presents a substantial reduction in analyst workload: only the flagged subset needs to be reviewed, and no true arrival is silently discarded. Full automation is not yet warranted given the precision, but the model is well-suited to a human-in-the-loop pipeline where it acts as a first-pass screener. A handful of machine annotated examples are inspected and discussed further in Appendix B.

SeisLM partially transferred its pretrained representations to N-wave picking (test $F_1 = 0.308$ with frozen CNN, 0.533 with full fine-tuning), suggesting that the transformer layers encode features that are at least partially relevant to this domain. However, SeisLM's parameter count ($\sim$90 M) is large relative to the 158 training examples available per fold, and the per-fold learning curves show a wider train–validation gap than PhaseNet scratch, consistent with mild overfitting. PhaseNet's compact U-Net ($\sim$100 k parameters) is better matched to this dataset size, and its convolutional inductive bias towards localized, time-varying features aligns naturally with the N-wave picking task.

Per-fold training and validation loss curves are shown in Fig. 4. All folds converged to a stable plateau in both training and validation loss, with no evidence of runaway overfitting (diverging validation loss). The train–validation gap stabilizes rather than widening, indicating that early stopping activated at or near the point of optimal generalization.

A limitation of the evaluation is that the model was only trained on 30 second windows constrained by dataset size: shorter windows keep the ratio of onset samples to background noises manageable during training, whereas longer windows would require proportionally more labeled data to avoid worsening class imbalance. This means that the current results demonstrate the model's ability to identify N-wave arrivals within a short pre-selected window rather than its performance as a fully automated picker operating on long, continuous, unsegmented records. As more annotated data becomes available, training on larger datasets would support longer time window samples, moving the model closer to the continuous monitoring systems required for full automation.

Another limitation caused by limited data is that the train–validation–

test splits were stratified by event rather than held out at the event level. Stations from both the Dragon CRS-32 and Shenzhou-15 events appear in both training and test sets, introducing some data leakage; because all stations within a single event record the same propagating N-wave, their waveforms share source characteristics (spectral content, amplitude envelope, duration) that a model could exploit without learning truly general N-wave features. The presence of two physically distinct events one year apart from each other, following different spacecraft and trajectories, partially mitigates this concern, as the model must generalize across at least two N-wave morphologies. Nevertheless, the reported metrics should be interpreted as performance on events similar to those in the training set, not as an estimate of performance on an entirely unseen reentry. A rigorous assessment of cross-event generalization would require holding out all stations from one event as a test set and training exclusively on the other, which is left for future work as additional reentry datasets become available. To support such future work, the manually labeled picks of the CRS-32 Cargo Dragon re-entry used for trajectory recovery and model training in this paper – to our knowledge, the first published set of seismic N-wave arrival picks for a controlled crew-class re-entry – are made available as supplementary material, providing a dataset for subsequent automation development. Note that the Shenzhou-15 picks from Fernando and Charalambous [8] are not publicly available and therefore not included. In a future operational system, models trained on sufficient data could be applied to streaming data from FDSN-compliant networks, automatically identifying candidate N-wave arrivals while flagging low-confidence detections for human review. The resulting picks would feed directly into the trajectory estimation workflow demonstrated here, enabling near-real-time localization of re-entry events.

4.5. Implications for re-entry monitoring

The contribution of 22 Raspberry Shake stations to the final dataset demonstrates that low-cost, citizen-operated seismic infrastructure can meaningfully complement traditional research-grade networks for re-entry localization. Their density in populated regions fills spatial gaps left by conventional stations, enabling a denser coverage of the sonic-boom footprint. At the same time, these instruments are prone to being noisier, exhibiting a median RMS noise floor value of 485.5 nm/s in stark contrast to the 47 nm/s picked up by the professional stations (see Fig. C.10). This difference further emphasizes the importance of spectrogram cross-referencing and calling for automated

quality-control procedures such as signal-to-noise ratio (SNR) thresholds to be applied alongside manual review.
More broadly, the entire analysis was conducted using only openly available seismic data, without access to operator telemetry, classified radar observations, or dedicated infrasound arrays. To the space community, this underscores an important point: current open-source seismic infrastructure is already capable of independent, continental-scale monitoring of atmospheric re-entry events at essentially zero marginal cost. Routine incorporation of seismic data into re-entry verification would provide a transparent, all-source check on predicted splashdown locations and could serve as a backup tracking method when radar or optical assets are unavailable.
These results show that the combination of open seismic data, citizen-science instruments, and deep-learning-based detection has the potential to transform re-entry monitoring from an ad hoc, manually intensive process into a routine, scalable capability. In other words, a method complementing existing radar and optical systems while remaining fully open and independent.

5. Conclusion

This study applied the seismoacoustic localization framework introduced by Fernando and Charalambous to the controlled re-entry of the SpaceX cargo Dragon C209 spacecraft on 25 May 2025. Using openly available waveform data from 95 stations across five networks, including 22 citizen-science Raspberry Shake instruments, we recovered a re-entry trajectory consistent with SpaceX's publicly communicated splashdown corridor off the coast of California.

As a preliminary step toward operational scalability, deep-learning approaches were also explored in the pipeline. Training PhaseNet from scratch yielded onset errors below 0.2 s on held-out stations, demonstrating that automated N-wave detection from small, single-event training sets is feasible. Scaling this approach across multiple re-entry events would reduce the manual workload and potentially enable near-real-time trajectory recovery from streaming seismic data.

The analysis demonstrates that existing, non-specialized seismic infrastructure is capable of providing independent characterization of human spaceflight, controlled re-entry events using only publicly available data. No access to operator telemetry, classified radar observations, or dedicated infrasound arrays (purpose-built networks of pressure sensors designed to detect atmospheric disturbances) is required. Unlike natural meteors and disintegrating space debris, a crew-class capsule is an intact, structurally rigid body descending under active guidance, sharing this property with sample return capsules [16, 42, 18, 20]. However, the crew-class capsule still differs in that it follows a propulsively controlled and guided descent from low-Earth-orbit velocities rather than an uncontrolled, ballistic trajectory at interplanetary (11–12 km/s) entry speeds. Seismoacoustic detection of atmospheric re-entries has also previously been demonstrated on meteoroid fireballs [14], uncontrolled re-entries for rocket stages [8], and the Space Shuttle Orbiters [12, 13], a comparably controlled, crewed vehicle; however, the Orbiter re-entries were flown under a government program for which detailed trajectory reconstructions were publicly available, allowing seismoacoustic detections to be validated against a known ground truth rather than used as an independent source of trajectory information. The present study is, to the authors' knowledge, the first published seismoacoustic tracking of a commercial crew-class capsule for which no such public telemetry exists: a vehicle type that will become increasingly common as NASA's Commercial Crew Program, commercial cargo resupply, and planned commercial space stations will lead to an increase of controlled re-entries conducted without the telemetry transparency of earlier government programs.

As both the total number of re-entries and the share of re-entries with limited public transparency are rising, it leaves regulators with few independent means to verify operator-reported outcomes: these include but are not limited to the actual re-entry ground track, the splashdown location, the extent of sonic boom exposure over populated areas, and whether fragmentation or debris shedding occurred as predicted by demisability analyses. The ability independently recover re-entry trajectories from open seismic data therefore carries several practical implications. For regulators, it provides a means to verify operator-reported re-entry outcomes without relying on proprietary telemetry or classified tracking data. For the scientific community, it allows systematic characterization of re-entry events, using already established global infrastructure. For spacecraft recovery operations, acoustic localization can help narrow the search area for capsule retrieval, particularly when radio telemetry is lost or delayed during the communications black-out phase of re-entry. As the rate of controlled and uncontrolled re-entries continues to grow, open-data methods such as the one demonstrated in this study offer a scalable, low-cost complementary option to established space situational awareness capabilities.

A limitation of the study is the absence of publicly available reference trajectory data against which to compute a quantitative localization error. Furthermore, the coastal splashdown resulted in an asymmetric station distribution with no ocean-side coverage. Future events, such as those from upcoming instrumented re-entry missions like ESA's DRACO (Destructive Re-entry Assessment Container Object) mission, scheduled for launch in 2027, offers a promising opportunity to address this limitation [43]. DRACO will carry a 150-200 kg satellite equipped with 200 sensors and 4 cameras that record temperature, pressure, heat flux, strain, altitude, and trajectory, and acceleration throughout the re-entry and break-up process. The data will be stored in an indestructible capsule that will survive the destruction, and be retrieved. Crucially, this telemetry will provide a precisely instrumented reference trajectory with known timing, altitude, and fragmentation sequence. Applying the seismoacoustic method demonstrated here to the DRACO re-entry and comparing with its ground-truth data would enable rigorous error quantification and further method validation.

Declaration of competing interest

The authors declare that they have no known competing financial interests or personal relationships that could have appeared to influence the work reported in this paper.

Declaration of generative AI and AI-assisted technologies in the manuscript preparation process

During the preparation of this work, the authors used ChatGPT and Claude in order to assist with Python/Matplotlib syntax for figure generation and to aid in structuring manuscript text. After using these tools, the authors reviewed and edited the content as needed and take full responsibility for the content of the published article.

CRediT author statement

Mikel Taotao Yu: Conceptualization, Methodology, Software, Validation, Formal Analysis, Investigation, Data Curation, Writing - Original Draft, Writing - Review and Editing, Visualization

Benjamin Fernando: Conceptualization, Methodology, Software, Validation, Formal Analysis, Resources, Writing - Review and Editing, Visualization, Supervision, Project Administration, Funding Acquisition

Funding source

Benjamin Fernando is funded by the Frederick Reines Distinguished Postdoctoral Fellowship in Experimental Science at the Los Alamos National Laboratory. This work was supported by the Space@Hopkins seed grant program at Johns Hopkins University.

Acknowledgements

Data were accessed from the NSF NGF data archive operated by EarthScope Consortium (NSF award 2435260). Computational resources for machine-learning model training were provided by DTU Computing Center (DCC) at the Technical University of Denmark [44].

Appendix A. Whitham's theory and N-wave duration

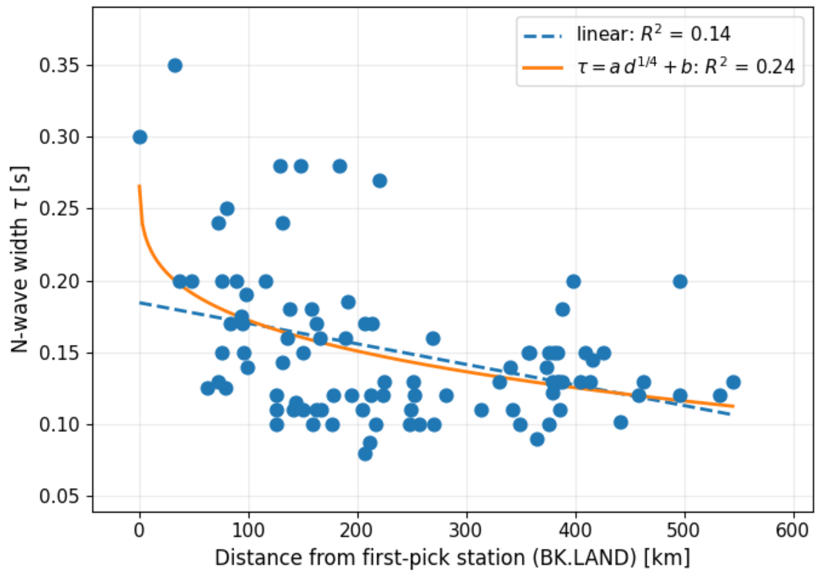

Figure A.5: **Scatter plot of N-wave duration against station downrange distance**. Both a linear and exponential fit was attempted on the data.

As an independent consistency check, N-wave durations τ were compared against distance proxies to test whether they follow the scaling predicted by Whitham's theory [22, 12]. Such a test is valuable as the propagation and coupling of the sonic boom to the ground depend on assumptions about the shock geometry and atmospheric propagation; a positive match would support those assumptions and help calibrate ground-coupling models for future events. Given a supersonic projectile in steady level flight, Whitham's theory gives $\tau \propto H^{1/4}$, where H is the perpendicular slant range from the source. When deceleration is significant, as in re-entry, the scaling is modified to approximately $\tau \propto H^{1/4}/U$ with U denoting the flight speed. This is because the N-wave duration is dependent on the Mach number M that varies with U. However, a direct test requires knowledge of the slant range H and the local Mach number, neither of which is available for this event given the lack of precise trajectory altitude data. Instead, three proxies were examined: downrange distance from the earliest-arriving station (BK.LAND) Fig. A.5, normalised haversine and time-based distances, and a projected altitude proxy assuming a constant descent angle, ranging from $R^2 = 0.04$ to $R^2 = 0.24$ (Appendix A, Fig. A.6, Fig. A.7).

The weak correlations reflect a common limitation: none of the proxies adequately captures the perpendicular slant range from the shock front to each station. Downrange distance from BK.LAND does not discriminate between along-track distance and cross-track offsets. As a consequence, two stations at the same downrange distance can receive the result of two different propagation paths. The altitude proxy partially to corrects for this by projecting stations perpendicularly onto the trajectory but assumes a constant descent angle which is unlikely to hold: during a controlled re-entry, the flight-path angle steepens as the vehicle decelerates. Additional composite distance metrics incorporating both along-track and cross-track components were explored but did not yield stronger correlations. This indicates that the proxy variables do not capture the true slant-range geometry required for a meaningful test of the theory.

All proxies tested produced a decreasing trend in τ with distance, opposite to the increase expected from a $H^{1/4}$ increase. The simplified scaling $\tau \propto H^{1/4}/U$ might predict a decrease if U decreases faster than $H^{1/4}$. However, this reasoning is incomplete given that the Mach number also evolves along the trajectory, and the full Whitham solution includes M in the fraction. Without altitude and Mach number data, a meaningful comparison to theory is not possible, and the sign of the observed trend cannot be interpreted properly.

Another obstacle is that the stations included in this study are located in the acoustic far field of the shockwave. For a transient pulse like an N-wave, the dominant frequency content is typically a few herts (1-10 Hz). The corresponding acoustic wavelength in air is $\lambda = c/f$; assuming a frequency of 5 Hz and sound speed of 330 ms^{-1} yields $\lambda \approx 66$ m. Within roughly one such wavelength of the shock front, the pressure signature preserves the true source-time function, i.e. the "ideal" N-wave shape and duration produced by the supersonic body. This region is called the acoustic near field.

As the wave propagates beyond one wavelength, roughly 66 m in this case, it enters the far field where several processes distort the pulse: atmospheric absorption removes higher frequencies, broadening the pulse. Refraction and scattering by temperature and wind gradients alter the waveform. Combined with multipathing, where different parts of the wavefront arrive at a station via different paths, the duration measured at a distant station is no longer representative of the source-generated N-wave length.

Most stations included in this study are located tens to hundreds of kilometers from the trajectory. The recorded N-wave durations are therefore heavily affected by source, path, and receiver effects, which can extend or shorten the observed pulse independently of the source. This large separation from the near field makes it impossible to retrieve the pure source duration required for a meaningful test of the Whitham scaling. Furthermore, the situation is compounded by the mixed station networks and types in the dataset: including both professionally installed broadband instruments and citizen-science instruments likely adds further scatter to duration measurements.

Therefore, a meaningful test of the Whitham scaling would require either known trajectory altitude and speeds or a denser near-field array with sensors placed within few acoustic wavelengths of the projected track.

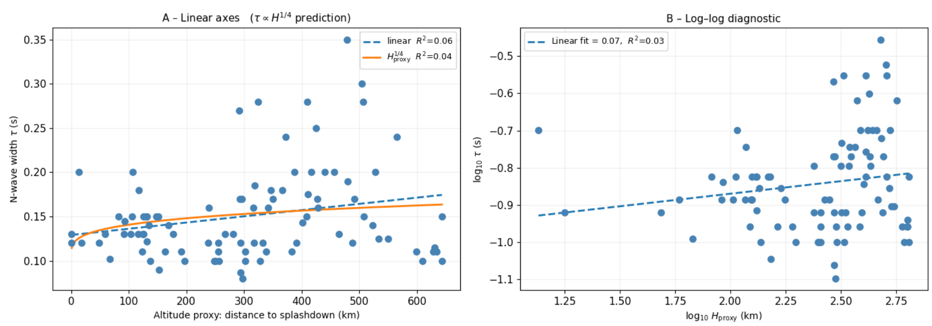

Figure A.6: N-wave duration τ against projected altitude proxy H_{proxy} (left, $R^2 = 0.04$) and corresponding log-log diagnostic (right, $R^2 = 0.03$). The altitude proxy assumes a constant descent angle and projects each station perpendicularly onto the approximate trajectory line.

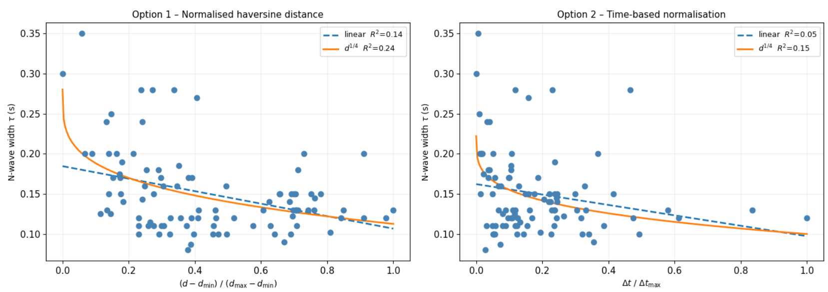

Figure A.7: N-wave duration τ against normalised haversine distance (left, $R^2 = 0.14$) and normalised time delay (right, $R^2 = 0.05$), with linear and quarter-power fits shown for comparison.

Appendix B. Representative PhaseNet Pick Examples

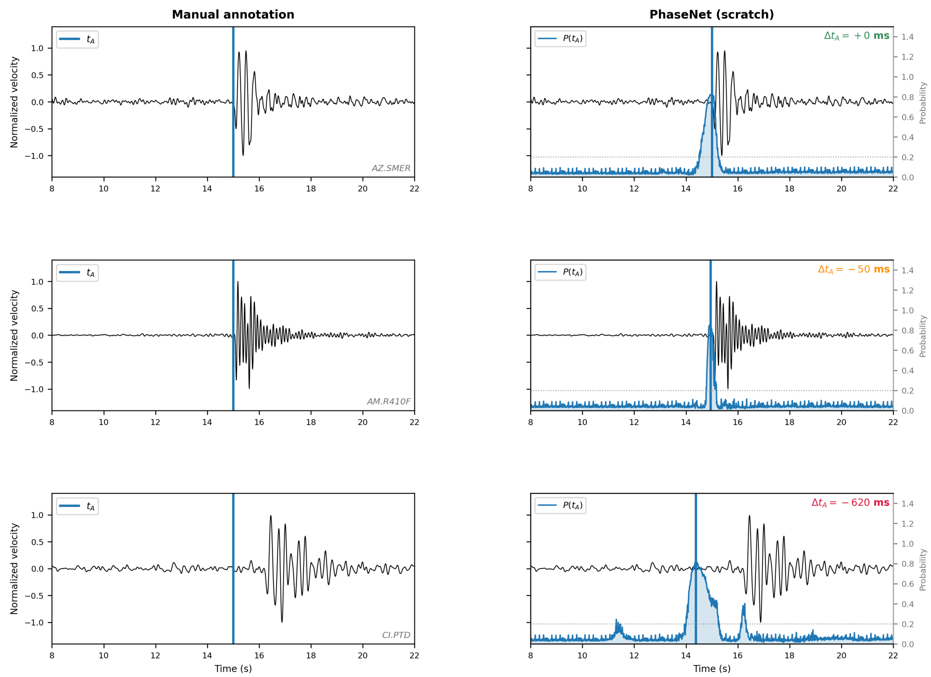

Figure B.8: Representative PhaseNet (scratch) picks on four held-out test stations spanning the observed quality range. Left panels show the manually annotated waveform with the N-wave onset t_A marked in blue. Right panels show the corresponding waveform overlaid with the model's $P(t_A)$ probability distribution output (shaded, right axis); the dashed horizontal line indicates the detection threshold of 0.20. The predicted pick (vertical blue line) and residual $\Delta t_A = t_A^{\text{pred}} - t_A^{\text{manual}}$ are shown in the upper right corner, colour-coded by accuracy: green ($|\Delta t_A| < 50$ ms), orange (< 300 ms), red (≥ 300 ms). All traces are displayed with a 0.5–8 Hz bandpass filter; station codes are given in italics in the bottom right corner of the manual annotations.

To further validate the PhaseNet (scratch) model results, a few model output examples were manually inspected after model training. Fig. B.8 displays four representative examples. For the seismogram of station AZ.SMER, the model predicted the exact same N-wave onset to within the 10 ms sampling resolution as the manual annotation. Additionally, the seismograms has a probability output $P(t_A)$ above 0.80 at the peak, suggesting not just high pick prediction accuracy but also high model confidence, even when the NN.SHP station data is noisy. For the third example, station AM.R410F, the model output was 50 milliseconds earlier than the manual annotation but still retained high pick confidence. As for the last seismogram, CI.PTD, the model predicted the wave onset to be 620 milliseconds earlier than the manual pick. Additionally, a smaller probability peak can be seen between 10 and 12 seconds, prompting further inspection.

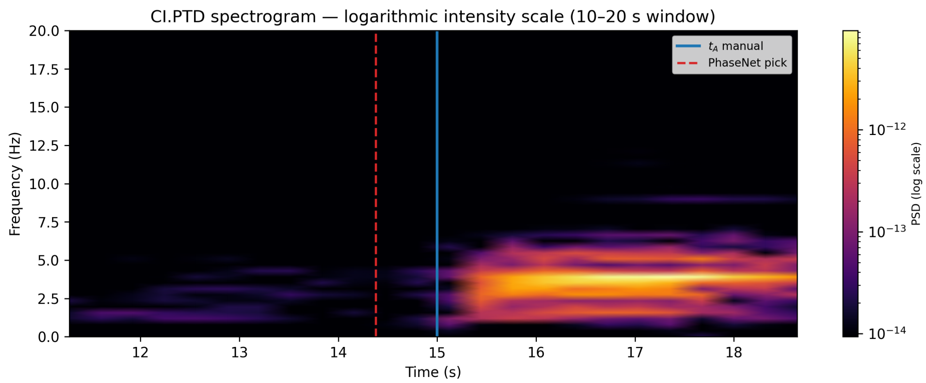

Figure B.9: Spectrogram of waveform data for the station CI.PTD. The manual annotation time t_A is marked with a vertical blue line, and PhaseNet (scratch) pick is marked with a dashed vertical red line. Note that the power spectral density (PSD) is displayed on a logarithmic scale

Fig. B.9 displays the spectrogram of the CI.PTD station. Weak spectral energy is present as narrow bands between 11 and 14 seconds. Combined with the smaller, but sudden vertical drop between 10 and 12 seconds in the corresponding seismogram where a smaller probability spike is found, it is plausible that this N-wave was preceded by a smaller boom from a smaller fragment of debris leading ahead of the spacecraft. It is therefore possible that PhaseNet (scratch) also picked up on this signal, prompting the smaller probability peak. However, sonic booms tend to be impulsive and therefore need to contain broad frequency content while the spectral energy looks narrow around 2 Hz. Therefore, it could also be local noise or sound belonging to something entirely unrelated. In summary, the model output for the station data of CI.PTD appears ambiguous and inconclusive.

Whether this constitutes a model failure or an incidental detection of a genuine secondary arrival remains unresolved without additional ground truth. Nevertheless, the result illustrates a broader challenge for automated N-wave pickers: when the input window contains any weak impulsive noise, the model may assign a non-trivial detection probability to it. This underscores the value of multi-station consistency checks when interpreting model output in practice, particularly for stations with low signal-to-noise ratios or ambiguous annotations.

Appendix C. Instrument Noise Performance: Raspberry Shake vs Professional Stations

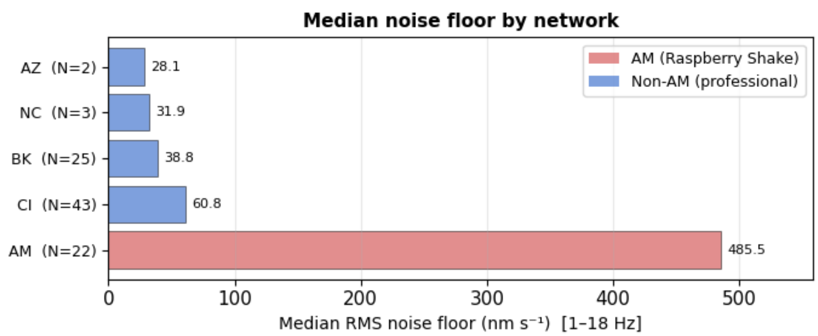

Figure C.10: Histogram bins of the median value of pre-arrival RMS noise floor in the 1–18 Hz velocity band for Raspberry Shake (AM network) and professional seismic stations (AZ, NC, BK, and CI). Noise is measured over a 30 second window, ending 30 second prior to the manually annotated N-wave onset (t_A), ensuring the estimate reflects contemporaneous background conditions rather than signal energy.

To compare the detection capabilities of the citizen-science Raspberry Shake instruments to the professional networks, we compare pre-arrival RMS noise floors in the 1–18 Hz passband used for both manual annotation and model training. As shown in Fig. C.10, the AM network exhibits a substantially higher median noise floor than the professional stations, consistent with the lower sensor grade, consumer-grade digitizers and typically non-ideal installation conditions: for instance, indoor placement and proximity to urban noise sources as is characteristic of Raspberry Shake deployments. This elevated noise level reduces the signal-to-noise ratio (SNR) of the N-wave picked up by AM stations which is also reflected in the higher proportion of unclear annotations assigned to them during manual annotation. Despite this limitation, 22 AM stations still had useful picks, comprising 23% of the final dataset used to construct Fig. 3. The inclusion of this many stations demonstrates that citizen-science instruments can contribute meaningfully to airwave detection when the signal amplitude is sufficient, while also highlighting the need for caution when interpreting model confidence scores at these sites.

References

[1] ESA Space Debris Office, Esa's annual space environment report, Tech. rep., European Space Agency (2025).
URL https://www.esa.int/Space_Safety/Space_Debris

[2] Federal Aviation Administration, Reentry disposal of satellites: Report to congress, Tech. rep., U.S. Department of Transportation, Washington, D.C. (2023).
URL https://www.faa.gov/sites/faa.gov/files/Report_to_Congress_Reentry_Disposal_of_Satellites.pdf

[3] P. D. Wilde, Aircraft safety and space vehicle hazards: How safe from space debris hazards will your future flights be?, Journal of Space Safety Engineering 12 (2) (2025) 299–311. doi:10.1016/j.jsse.2025.03.006.
URL https://www.sciencedirect.com/science/article/pii/S2468896725000187

[4] T. Schildknecht, Optical surveys for space debris, 14 (1) (2007) 41–111. doi:10.1007/s00159-006-0003-9.
URL https://ui.adsabs.harvard.edu/abs/2007A&ARv..14...41S

[5] D. Mehrholz, L. Leushacke, W. Flury, R. Jehn, H. Klinkrad, M. Landgraf, Detecting, tracking and imaging space debris, Fraunhofer FHR 109 (02 2002).

[6] C. Pardini, L. Anselmo, Assessing the risk and the uncertainty affecting the uncontrolled re-entry of manmade space objects, Journal of Space Safety Engineering 5 (1) (2018) 46–62. doi:10.1016/j.jsse.2018.01.003.
URL https://www.sciencedirect.com/science/article/pii/S2468896717301003

[7] T. Neidhart, K. Miljković, E. K. Sansom, H. A. R. Devillepoix, T. Kawamura, J.-L. Dimech, M. A. Wieczorek, P. A. Bland, Statistical analysis

of fireballs: Seismic signature survey, Publications of the Astronomical Society of Australia 38 (2021) e016. doi:10.1017/pasa.2021.11.

[8] B. Fernando, C. Charalambous, Reentry and disintegration dynamics of space debris tracked using seismic data, Science 391 (6783) (2026) 412–416. arXiv:https://www.science.org/doi/pdf/10.1126/science.adz4676, doi:10.1126/science.adz4676.
URL https://www.science.org/doi/abs/10.1126/science.adz4676

[9] NASA, Spacex dragon splashes down off the coast of california (2025).
URL https://www.nasa.gov/blogs/spacestation/2025/05/25/spacex-dragon-splashes-down-off-the-coast-of-california/

[10] SpaceX, Crs-32 mission (2025).
URL https://www.spacex.com/launches/crs-32

[11] SpaceX, Dragon vehicle (2026).
URL https://www.spacex.com/vehicles/dragon

[12] H. Kanamori, J. Mori, B. Sturtevant, D. L. Anderson, T. Heaton, Seismic excitation by space shuttles, Shock Waves 2 (1992) 89–96. doi:10.1007/BF01415896.

[13] A. Qamar, Space shuttle and meteroid–tracking supersonic objects in the atmosphere with seismographs, Seismological Research Letters 66 (5) (1995) 6–12.

[14] E. A. Silber, M. Boslough, W. K. Hocking, M. Gritsevich, R. W. Whitaker, Physics of meteor generated shock waves in the earth's atmosphere – a review, Advances in Space Research 62 (3) (2018) 489–532. doi:10.1016/j.asr.2018.05.010.
URL https://www.sciencedirect.com/science/article/pii/S027311771830406X

[15] D. Eickhoff, J. P. Föst, J. R. R. Ritter, Re-entry and burn up of starlink-2382 satellite: estimating trajectory and ablation coefficient from acoustic and coupled seismic waves, Geophysical Journal International 246 (2) (2026) ggag182. arXiv:https://academic.oup.com/gji/article-pdf/246/2/ggag182/68279360/ggag182.pdf, doi:

10.1093/gji/ggag182.
URL https://doi.org/10.1093/gji/ggag182

[16] D. O. ReVELLE, W. EDWARDS, T. D. SANDOVAL, Genesis—an artificial, low velocity "meteor" fall and recovery: September 8, 2004, Meteoritics & Planetary Science 40 (6) (2005) 895–916. arXiv:https://onlinelibrary.wiley.com/doi/pdf/10.1111/j.1945-5100.2005.tb00162.x, doi:https://doi.org/10.1111/j.1945-5100.2005.tb00162.x.
URL https://onlinelibrary.wiley.com/doi/abs/10.1111/j.1945-5100.2005.tb00162.x

[17] W. N. Edwards, D. W. Eaton, P. J. McCausland, D. O. ReVelle, P. G. Brown, Calibrating infrasonic to seismic coupling using the stardust sample return capsule shockwave: Implications for seismic observations of meteors, Journal of Geophysical Research: Solid Earth 112 (B10) (2007). arXiv:https://agupubs.onlinelibrary.wiley.com/doi/pdf/10.1029/2006JB004621, doi:https://doi.org/10.1029/2006JB004621.
URL https://agupubs.onlinelibrary.wiley.com/doi/abs/10.1029/2006JB004621

[18] M.-y. Yamamoto, Y. Ishihara, Y. Hiramatsu, K. Kitamura, M. Ueda, Y. Shiba, M. Furumoto, K. Fujita, Detection of acoustic/infrasonic/seismic waves generated by hypersonic re-entry of the hayabusa capsule and fragmented parts of the spacecraft, Publications of the Astronomical Society of Japan 63 (5) (2011) 971–978. arXiv:https://academic.oup.com/pasj/article-pdf/63/5/971/61209114/pasj_63_5_971.pdf, doi:10.1093/pasj/63.5.971.
URL https://doi.org/10.1093/pasj/63.5.971

[19] E. A. Silber, D. C. Bowman, C. G. Carr, D. P. Eisenberg, B. R. Elbing, B. Fernando, M. A. Garcés, R. Haaser, S. Krishnamoorthy, C. A. Langston, Y. Nishikawa, J. Webster, J. F. Anderson, S. Arrowsmith, S. Bazargan, L. Beardslee, B. Beck, J. W. Bishop, P. Blom, G. Bracht, D. L. Chichester, A. Christe, J. Clarke, K. Cummins, J. Cutts, L. Danielson, C. Donahue, K. Eack, M. Fleigle, D. Fox, A. Goel, D. Green, Y. Hasumi, C. Hayward, D. Hicks, J. Hix, S. Horton, E. Hough, D. P. Huber, M. A. Hunt, J. Inman, S. M. A. Islam, J. Izraelevitz, J. D. Jacob,

J. Johnson, R. J. KC, A. Komjathy, E. Lam, J. LaPierre, K. Lewis, R. D. Lewis, P. Liu, L. Martire, M. McCleary, E. A. McGhee, I. Mitra, A. Nag, L. Ocampo Giraldo, K. Pearson, M. Plaisir, S. K. Popenhagen, H. Rassoul, M. Ronac Giannone, M. Samnani, N. Schmerr, K. Spillman, G. Srinivas, S. K. Takazawa, A. Tempert, R. Turley, C. Van Beek, L. Viens, O. A. Walsh, N. Weinstein, R. White, B. Williams, T. C. Wilson, S. Wyckoff, M.-y. Yamamoto, Z. Yap, T. Yoshiyama, C. Zeiler, Geophysical observations of the 2023 september 24 osiris-rex sample return capsule reentry, The Planetary Science Journal 5 (9) (2024) 213. doi:10.3847/PSJ/ad5b5e.
URL https://doi.org/10.3847/PSJ/ad5b5e

[20] E. A. Silber, D. C. Bowman, S. Albert, A review of infrasound and seismic observations of sample return capsules since the end of the apollo era in anticipation of the osiris-rex arrival, Atmosphere 14 (10) (2023). doi:10.3390/atmos14101473.
URL https://www.mdpi.com/2073-4433/14/10/1473

[21] J. W. Bishop, P. Blom, C. Carr, J. Webster, An infrasound source analysis of the osiris-rex sample return capsule hypersonic re-entry, The Journal of the Acoustical Society of America 158 (6) (2025) 4637–4650. doi:10.1121/10.0041857.

[22] G. B. Whitham, Linear and Nonlinear Waves, John Wiley and Sons, New York, 1974.

[23] M. Beyreuther, R. Barsch, L. Krischer, T. Megies, Y. Behr, J. Wassermann, Obspy: A python toolbox for seismology, Seismological Research Letters 81 (3) (May/June 2010) 530–533. arXiv:http://srl.geoscienceworld.org/content/81/3/530.full.pdf+html, doi:10.1785/gssrl.81.3.530.
URL http://www.seismosoc.org/publications/SRL/SRL_81/srl_81-3_es/

[24] L. Krischer, T. Megies, R. Barsch, M. Beyreuther, T. Lecocq, C. Caudron, J. Wassermann, Obspy: a bridge for seismology into the scientific python ecosystem, Computational Science Discovery 8 (1) (2015) 014003. doi:10.1088/1749-4699/8/1/014003.
URL https://doi.org/10.1088/1749-4699/8/1/014003

[25] EarthScope Consortium, Nsf national geophysical facility (ngf), nSF award 2435260 (2025).
URL https://www.earthscope.org

[26] Northern California Earthquake Data Center, Northern california earthquake data center (2014). doi:10.7932/NCEDC.

[27] Southern California Earthquake Data Center, Southern california earthquake data center (2013). doi:10.7909/C3WD3xH1.

[28] California Institute of Technology and U.S. Geological Survey, Southern california seismic network (1926). doi:10.7914/SN/CI.

[29] Northern California Earthquake Data Center, Berkeley digital seismic network (bdsn) (2014). doi:10.7932/BDSN.

[30] Frank Vernon, Anza regional network (1982). doi:10.7914/SN/AZ.
URL https://www.fdsn.org/networks/detail/AZ/

[31] U.S. Geological Survey, Usgs northern california seismic network (1967). doi:10.7914/SN/NC.

[32] Raspberry Shake S.A., Raspberry shake network (2016). doi:10.7914/SN/AM.

[33] J. Bigun, G. H. Granlund, Optimal orientation detection of linear symmetry, in: IEEE International Conference on Computer Vision, 1987.
URL https://api.semanticscholar.org/CorpusID:117745987

[34] P. Bakker, L. van Vliet, P. Verbeek, Edge preserving orientation adaptive filtering, in: Proceedings. 1999 IEEE Computer Society Conference on Computer Vision and Pattern Recognition (Cat. No PR00149), Vol. 1, 1999, pp. 535–540 Vol. 1. doi:10.1109/CVPR.1999.786989.

[35] D. Eickhoff, R. Ostermeier, J. Ritter, Seismo-acoustic meteoroid observation recording database (smord): A global dataset and deep-learning phase picker for meteoroid-generated air-to-ground coupled seismic waves, Seismica 5 (2) (Jul. 2026). doi:10.26443/seismica.v5i2.2551.
URL https://seismica.library.mcgill.ca/article/view/2551

[36] T. Liu, J. Münchmeyer, L. Laurenti, C. Marone, M. V. de Hoop, I. Dokmanić, Seislm: a foundation model for seismic waveforms (2024). arXiv:2410.15765.
URL https://arxiv.org/abs/2410.15765

[37] W. Zhu, G. C. Beroza, Phasenet: a deep-neural-network-based seismic arrival-time picking method, Geophysical Journal International 216 (1) (2019) 261–273. arXiv:https://academic.oup.com/gji/article/216/1/261/5129142, doi:10.1093/gji/ggy423.
URL https://doi.org/10.1093/gji/ggy423

[38] C. R. Harris, K. J. Millman, S. J. van der Walt, R. Gommers, P. Virtanen, D. Cournapeau, E. Wieser, J. Taylor, S. Berg, N. J. Smith, R. Kern, M. Picus, S. Hoyer, M. H. van Kerkwijk, M. Brett, A. Haldane, J. F. del Río, M. Wiebe, P. Peterson, P. Gérard-Marchant, K. Sheppard, T. Reddy, W. Weckesser, H. Abbasi, C. Gohlke, T. E. Oliphant, Array programming with numpy, Nature 585 (7825) (2020) 357–362. doi:10.1038/s41586-020-2649-2.
URL http://dx.doi.org/10.1038/s41586-020-2649-2

[39] J. D. Hunter, Matplotlib: A 2d graphics environment, Computing in Science & Engineering 9 (3) (2007) 90–95. doi:10.1109/MCSE.2007.55.

[40] Met Office, Cartopy: a cartographic python library with a matplotlib interface (2015).
URL https://cartopy.readthedocs.io

[41] SpaceX, Dragon is on track to reenter earth's atmosphere and splash down off the southern coast of california near oceanside, posted on X (Twitter) (2024).
URL https://x.com/SpaceX/status/1926500301382537540

[42] D. O. ReVelle, W. N. Edwards, Stardust—an artificial, low-velocity "meteor" fall and recovery: 15 january 2006, Meteoritics & Planetary Science 42 (2) (2007) 271–299. arXiv:https://onlinelibrary.wiley.com/doi/pdf/10.1111/j.1945-5100.2007.tb00232.x, doi:https://doi.org/10.1111/j.1945-5100.2007.tb00232.x.
URL https://onlinelibrary.wiley.com/doi/abs/10.1111/j.1945-5100.2007.tb00232.x

[43] European Space Agency, Draco mission: Made for destruction, accessed: 2026-05-27 (Sep. 2024).
URL https://www.esa.int/Space_Safety/Draco_mission_made_for_destruction

[44] DTU Computing Center, DTU Computing Center resources (2026). doi:10.48714/DTU.HPC.0001.
URL https://doi.org/10.48714/DTU.HPC.0001